Probing scattering mechanisms with symmetric quantum cascade lasers

Christoph Deutsch,[1,*] Hermann Detz,[2] Tobias Zederbauer,[2] Aaron M. Andrews,[2] Pavel Klang,[2] Tillman Kubis,[3] Gerhard Klimeck[3], Manfred E. Schuster,[4] Werner Schrenk[2], G. Strasser[2], and K. Unterrainer[1]

[1]*Photonics Institute and Center for Micro- and Nanostructures, Vienna University of Technology, Gusshausstrasse 27–29, 1040 Vienna, Austria*
[2]*Institute of Solid-State Electronics and Center for Micro- and Nanostructures, Vienna University of Technology, Floragasse 7, 1040 Vienna, Austria*
[3]*Network for Computational Nanotechnology, Purdue University, 207 S Martin Jischke, West Lafayette, Indiana 47906, USA*
[4]*Fritz-Haber-Institut der Max-Planck-Gesellschaft, Faradayweg 4–6, 14195 Berlin, Germany*
[*]*christoph.deutsch@tuwien.ac.at*

Abstract: A unique feature of quantum cascade lasers is their unipolar transport. We exploit this feature and designed nominally symmetric active regions for terahertz quantum cascade lasers, which should yield equal performance with either bias polarity. However, symmetric devices realized in the InGaAs/GaAsSb material system exhibit a strongly polarity-dependent performance due to different elastic scattering rates, which makes them an ideal tool to study their importance. In the case of an InGaAs/GaAsSb heterostructure, the enhanced interface asymmetry can even lead to undirectionally working devices, although the nominal band structure is symmetric. The results are also a direct experimental proof that interface roughness scattering has a major impact on transport/lasing performance.

©2012 Optical Society of America

OCIS codes: (000.0000) General; (000.2700) General science.

References and links

1. B. Williams, “Terahertz quantum-cascade lasers,” Nat. Photonics **1**, 517 (2007).
2. F. Capasso, “High-performance midinfrared quantum cascade lasers”, Opt. Eng. 49, 111102 (2010).
3. C. Gmachl, A. Tredicucci, D. L. Sivco, A. L. Hutchinson, F. Capasso, and A. Y. Cho, “Bidirectional semiconductor laser”, Science **286**, 749 (1999).
4. L. Lever, N. M. Hinchcliffe, S. P. Khanna, P. Dean, Z. Ikonic, C. A. Evans, A. G. Davies, P. Harrison, E. H. Linfield, and R. W. Kelsall, “Terahertz ambipolar dual-wavelength quantum cascade laser”, Opt. Express **17**, 19926 (2009).
5. T. Kubis, C. Yeh, P. Vogl, A. Benz, G. Fasching, and C. Deutsch, “Theory of nonequilibrium quantum transport and energy dissipation in terahertz quantum cascade lasers”, Phys. Rev. B **79**, 195323 (2009).
6. R. Nelander and A. Wacker, “Temperature dependence of gain profile for terahertz quantum cascade lasers”, Appl. Phys. Lett. **92**, 081102 (2008).
7. C. Jirauschek and Paolo Lugli, “Monte-Carlo-based spectral gain analysis for terahertz quantum cascade lasers”, J. Appl. Phys. **105**, 123102 (2009).
8. A. Bismuto, R. Terazzi, M. Beck, and J. Faist, “Influence of the growth temperature on the performance of strain-balanced quantum cascade lasers”, Appl. Phys. Lett. **98**, 091105 (2011).
9. Y. Chiu, Y. Dikmelik, P. Q. Liu, N. L. Aung, J. B. Khurgin, and C. F. Gmachl, “Importance of interface roughness induced intersubband scattering in mid-infrared quantum cascade lasers”, Appl. Phys. Lett. **101**, 171117 (2012).
10. M. P. Semtsiv, Y. Flores, M. Chashnikova, G. Monastyrskyi, and W. T. Masselink, “Low-threshold intersubband laser based on interface-scattering-rate engineering”, Appl. Phys. Lett. 100, 163502 (2012).
11. P. Q. Liu, A. J. Hoffman, M. D. Escarra, K. J. Franz, J. B. Khurgin, Y. Dikmelik, X. Wang, J.-Y. Fan, and C. F. Gmachl, “Highly power-efficient quantum cascade lasers”, Nat. Photonics **4**, 95 (2010).

12. S. Fathololoumi, E. Dupont, C. W. I. Chan, Z. R. Wasilewski, S. R. Laframboise, D. Ban, A. Mátyás, C. Jirauschek, Q. Hu, and H. C. Liu, “Terahertz quantum cascade lasers operating up to 200 K with optimized oscillator strength and improved injection tunneling”, Opt. Express **20**, 3866 (2012).
13. H. Luo, S. R. Laframboise, Z. R. Wasilewski, G. C. Aers, H. C. Liu, “Terahertz quantum-cascade lasers based on a three-well active module”, Appl. Phys. Lett. **90**, 041112 (2007).
14. C. Deutsch, A. Benz, H. Detz, P. Klang, M. Nobile, A. M. Andrews, W. Schrenk, T. Kubis, P. Vogl, G. Strasser, and K. Unterrainer, “Terahertz quantum cascade lasers based on type II InGaAs/GaAsSb/InP”, Appl. Phys. Lett. **97**, 261110 (2010).
15. M. Nobile, H. Detz, E. Mujagic, A. M. Andrews, P. Klang, W. Schrenk, and G. Strasser, “Midinfrared intersubband absorption in InGaAs/GaAsSb multiple quantum wells”, Appl. Phys. Lett. **95**, 041102 (2009).
16. R. M. Feenstra, D. A. Collins, D. Z.-Y. Ting, M. W. Wang, and T. C. McGill, “Interface roughness and asymmetry in InAs/GaSb superlattices studied by scanning tunneling microscopy”, Phys. Rev. Lett. **72**, 2749 (1994).
17. T. Unuma, T. Takahashi, T. Noda, M. Yoshita, H. Sakaki, M. Baba, and H. Akiyama, “Effects of interface roughness and phonon scattering on intersubband absorption linewidth in a GaAs quantum well”, Appl. Phys. Lett. **78**, 3448 (2001).
18. T. Ando, A. B. Fowler, and F. Stern, “Electronic properties of two-dimensional systems”, Rev. Mod. Phys. **54**, 437 (1982).
19. C. Deutsch, APL published soon

---

1. Introduction

The emission wavelength of a quantum cascade lasers (QCLs), currently ranging from the mid-infrared to the terahertz (THz) spectral region (3–300 µm) [1,2], can be engineered by designing subband levels in a semiconductor heterostructure. This unique feature is usually referred as band structure engineering. The second exclusive property of QCLs is their unipolarity. This feature allows the realization of bidirectional devices [3,4]. In this work, we show how such bidirectional devices can be used to gain a deeper understanding of elastic scattering in an active region of a QCL.

In fact, the transport in QCLs is not fully understood yet and transport simulations are especially controversial for active regions used in THz QCLs. While longitudinal optical (LO) phonon scattering is known to be crucial in mid-infrared and, at elevated temperatures, in THz QCLs, the influence of elastic scattering mechanisms is not well understood. Low temperature transport in THz QCLs is a complex interplay of coherent tunneling, elastic scattering and LO phonon scattering. However, which elastic scattering mechanisms are dominant and which one are negligible is disputed. Theoretical modeling has been focusing on interface roughness, impurity and electron-electron scattering [5–7]. Even for the very mature mid-infrared QCL technology, elastic scattering due to interface roughness is put in the focus of research to gain considerable device improvements nowadays [8–10]. THz QCL performance is expected to be even more susceptible to elastic scattering since the optical transition energy is well below the LO phonon energy. The knowledge of the origin and influence of scattering mechanisms is going to be important in the race for higher operating temperatures, as they decrease/broaden the optical gain. Currently, the only successful strategy towards higher operating temperatures is to increase the optical gain by careful design optimizations [11], avoiding elastic scattering could be the next step.

The experimental challenge lies in the direct observation of the influence of a certain scattering mechanism in QCLs. For this purpose we exploit a feature of QCLs, which is their unipolar carrier transport. Combined with a high degree of freedom due to band structure engineering, one can design bidirectional, dual wavelength or nominally symmetric active regions. An early work on mid-infrared QCLs was focused on dual wavelength operation with either bias polarity and a symmetric active region was merely demonstrated as a proof of principle [3].

2. Symmetric active regions

We designed a series of three symmetric THz QCL active regions based on the three-well phonon depletion scheme in the InGaAs/GaAsSb material system [12,13].

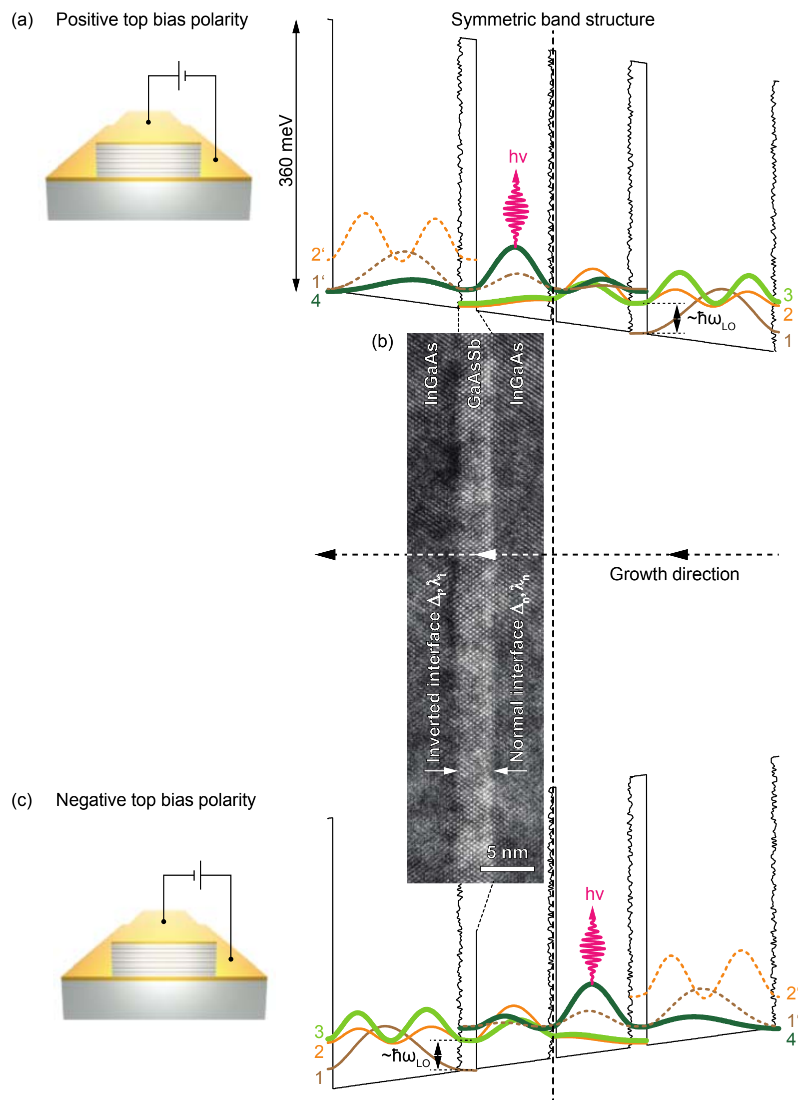

Fig. 1. Nominally symmetric active region of a terahertz quantum cascade laser biased with either bias polarity. The symmetry is broken by the different quality of the normal and inverted interface with respect to the growth direction. The inverted interfaces are sketched as a rough line in the band structure. (a) Positive top bias polarity results in an electron flow incident on the inverted interfaces. (b) The cross-sectional TEM picture confirms the interface asymmetry in the InGaAs/GaAsSb material system and the enhanced roughness of inverted interface. (c) Negative polarity reverses the current flow and electrons are moving against the normal interfaces. Therefore, the influence of interface roughness scattering can be studied by simply switching between the bias polarities.

The band structures are modeled with an effective mass 1D Schrödinger solver and material parameters are used from Ref. 14. The active region of the initial design (sample 1), biased with either polarity, is shown in Figure 1(a) and (c). Samples 2 and 3 are improved versions of sample 1 and the modifications are described in Chapter 4 and Figure 2. In theory, the bias polarity makes no difference and will result in equal device performance. However, the two sides of the GaAsSb barrier are not symmetric due to the actual growth of the heterostructure. This effect of asymmetric interface qualities is known to be pronounced in the 6.1 A material family and related alloys, when different group V materials like As and Sb are used for the

growth of the semiconductor heterostructure [16]. The same effect is also found in the presented material system, InGaAs/GaAsSb latticed matched to InP. A high-resolution cross-sectional TEM picture of the 3 nm GaAsSb barrier, shown in Figure 1(b), reveals the increased roughness of the inverted interface. The expression normal and inverted are commonly used in 2DEG structures for the two kind of interfaces, where the normal interface describes the switching from the well to barrier material in the conduction band during growth (from InGaAs to GaAsSb in this case) and vice versa for the inverted. The interface asymmetry with respect to the growth direction is also sketched in the band structures, where the rough lines indicate the inverted interfaces. By applying a bias, the nominally symmetric band structure becomes asymmetric and depending on the polarity, the wave functions are either pushed to the rougher or smoother interfaces, i.e. the subbands exhibit a different value of probability at the position of the two interfaces. A simple comparison of the probability density of the upper and lower laser level between the two interfaces yields a difference of ~30%. The consequence is different scattering rates between the two operating directions. The interface roughness scattering rate has to be split into two parts, accounting for the difference in step height $\Delta_{inv}, \Delta_{norm}$ and correlation length $\Lambda_{inv}, \Lambda_{norm}$ of the normal and inverted interface [9,17,18]:

$$\tau_{IR}^{-1} = \frac{\pi m_e}{\hbar^3} \delta U^2 \left(\sum_{inv} \Lambda_{inv}^2 \Delta_{inv}^2 \psi_i^2(z_{inv}) \psi_f^2(z_{inv}) e^{-\frac{\Delta_{inv}^2 q_{if}}{4}} + \sum_{norm} \Lambda_{norm}^2 \Delta_{norm}^2 \psi_i^2(z_{norm}) \psi_f^2(z_{norm}) e^{-\frac{\Delta_{norm}^2 q_{if}}{4}} \right) \quad 1$$

Here, m_e is the electron effective mass, δU is the conduction band offset, ψ_i^2, ψ_f^2 are the probability values of the initial and final subband at the position z_{inv}, z_{norm} of the respective interface and q_{if} is the absolute value of the 2D scattering vector.

3. Fabrication and experimental setup

The active region designs are grown with a Riber 32 on InP with a substrate tempature of 470–480°C. Symmetric InGaAs contact layeres doped to 7×10^{18} cm^{-3} are grown bottom and top. The total active region thickness is ~10 µm (170 periods). 10/1000 nm Ti/Au metal layers are deposited on the sample wafers and on n+ GaAs host substrates. After wafer bonding using a thermo-compression method, the original substrate is removed by mechanical polishing and selective wet etching. Standard lithography is used to define the top contact/waveguide and is followed by metallization of 10/500 nm Ti/Au. Subsequently, ridges are dry-etched with an inductively coupled plasma reactive ion etcher using an SiCl4:Ar chemistry. The top contact is protected by an additional SiN or Ni layer and acts as a self-aligned etch mask. Unlike commonly used wet-etching, dry etching also guarantees vertical sidewalls and a symmetric geometry of the device. Typical device dimensions are 0.5–1 mm by 40–90 µm.

The fabricated devices are indium soldered on a copper submount, wire-bonded and mounted on the cold finger of a helium flow cryostat. Light emission was collected using an off-axis parabolic mirror, sent through an FTIR spectrometer and detected with a DTGS detector. Absolute power values are measured with a calibrated thermopile detector (Dexter 6M) under vacuum conditions, mounted at a distance of 5–10 mm from the laser facet inside the cryostat. The detector element has a diameter of 6 mm. Light-current-voltage (LIV) curves and spectra are recorded in pulsed mode, with a pulse duration of 200 ns.

4. Experimental results and discussion

Figure 2(a) summarizes the design parameters and major differences between the 3 tested samples. The bidirectional LIV characteristics of sample 1 are shown Figure 2(b). Although the active region design, as well as contacts and device geometry, is completely symmetric, lasing is just observed with negative top bias polarity with a threshold current density of 0.62 kA/cm^2.

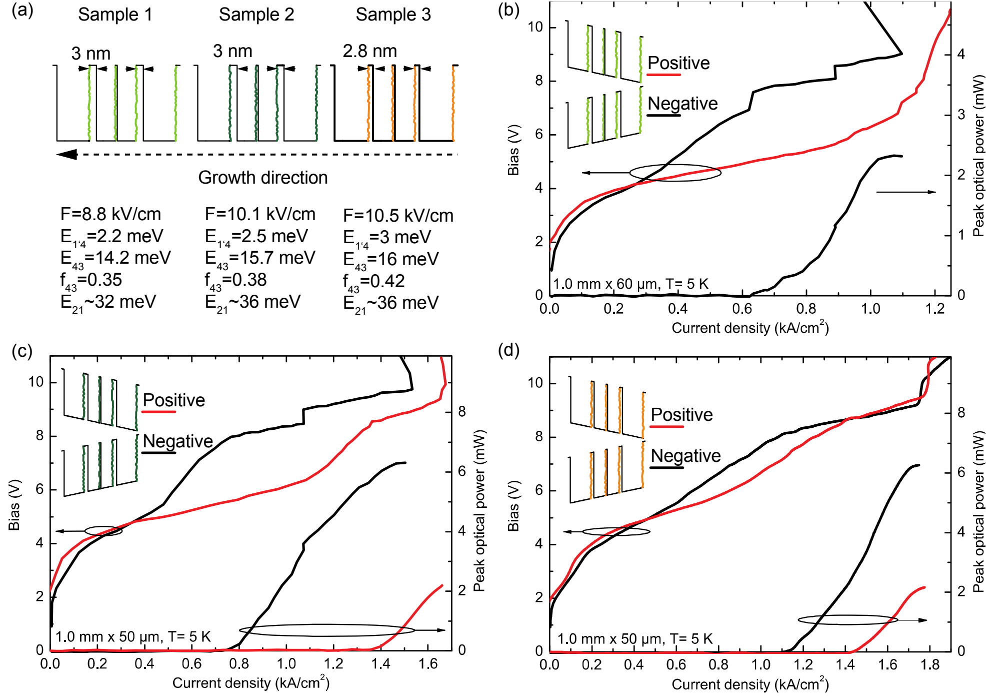

Fig. 1. Comparison of the different active region designs and light-current-voltage characteristics of each measured with both operating polarities. (a) The layer sequence of the sample 1 is **3.0**/14.0/**1.0**/14.0/**3.0**/2.0/22.0/2.0 nm. For sample 2 the layer sequence was modified to **3.0**/13.3/**1.0**/13.3/**3.0**/2.0/18.8/2.0 nm, which results in a better depletion of the lower laser level due to optimized subband alignment and energy separation (E_{21}). Sample 3 employs thinner injection/extraction barriers for stronger tunneling coupling. The layer sequence is **2.8**/13.0/**0.9**/13.0/**2.8**/1.9/20.5/1.9 nm. Barriers are in bold fonts and the doped section is underlined. (b) Sample 1 only shows lasing for negative polarity. (c) Sample 2 works with both polarities but exhibits a significant transport and performance difference. (d) Thinner barriers in sample 3 enhance the tunneling coupling and 'reduce the transport asymmetry.

In this case, the electron transport occurs in growth direction and electrons "see" the normal, smoother interfaces, resulting in a decreased interface roughness scattering compared to the opposite operating direction. The enhanced interface roughness scattering with positive bias causes increased leakage in the IV beyond 4 V. More important though, the upper state lifetime τ_4 is also dramatically decreased and the optical gain cannot overcome the waveguide losses. Lasing with negative bias is observed up to a maximum temperature of 105 K. By redesigning the subband level alignment and energy separation of level 1 and 2 for resonant depletion, the optimized sample 2 shows also lasing for positive polarity, presented in Figure 2(c). However, the IV asymmetry remains basically unchanged with a higher leakage current and hence higher threshold for positive polarity. The reduced optical output power reflects the reduced upper state lifetime τ_4. For a more significant comparison of the polarity-dependent performance, we characterized 4 devices. The average values and their ratio including standard deviation are summed up in Table 1. Sample 2 exhibits a –43% reduced threshold a +238% higher output power and a +20% higher operating temperature for negative polarity. The peculiar kinks, visible in the negative polarity IV of sample 1 and 2, vary from device to device and are attributed to the formation of high field domains in the active region. The purpose of sample 3 is to study the influence of a thinner injection/extraction barrier on the performance difference. Figure 2(d) shows the LIV characteristics of sample 3. The IV exhibits a reduced asymmetry and the threshold current difference is reduced to –19%.

Table 1. Performance comparison of 3 different symmetric active regions and bias polarity

Sample	Positive top bias		Negative top bias		Ratio Negative/positive		
	J_{th} (kA/cm^2)	T_{max} (K)	J_{th} (kA/cm^2)	T_{max} (K)	J_{th}	T_{max}	P_{peak}
1	-	-	0.54	105	-	-	-
2	1.43	103	0.81	124	0.57±0.03	1.20±0.04	2.38±0.37
3	1.34	103	1.08	134	0.81±0.04	1.32±0.15	2.86±0.28

4 devices of sample 2 and 3 have been measured for a meaningful comparison between the two operating directions. The average values for threshold current density J_{th}, maximum operating temperature T_{max} and the ratio of them are listed. Peak optical output power P_{peak} is only provided as a ratio since the absolute values strongly depend on the device dimensions. The standard deviation is also provided for the ratios and shows that the difference is not within error bars. J_{th} and P_{peak} have been measured at 5K.

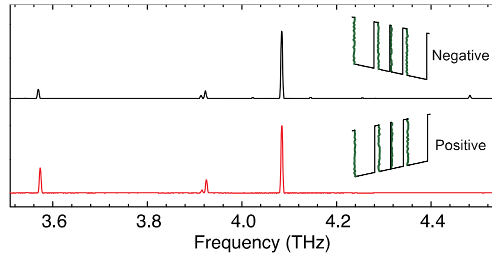

Figure 3. Normalized spectra of sample 2 recorded in either bias polarity at the maximum optical output. The main lasing modes are observed in both spectra. It indicates that the spectral position of the gain is not influenced by the applied polarity and the resulting subband level alignment/spacing is identical.

Thinner barriers give stronger tunneling coupling, which means that coherent transport plays a more dominant role compared to elastic scattering in this structure. The change of the barrier width from 3 nm to 2.8 nm in sample 3 yields an anticrossing energy of 3 meV. However, the difference for the upper state lifetime τ_4 remains unaffected and causes a similar difference for the output power compared to sample 2, which is +286% for negative polarity. Sample 3 shows the best temperature performance of 134 K for negative polarity, 32% higher than for positive polarity. Figure 3 shows the positive and negative polarity spectra of a representative device of sample 2. The spectra are recorded at the maximum output power and relatively broadband, which is attributed to the generally rougher interfaces compared to GaAs/AlGaAs [19]. More interesting though is the similarity of the recorded spectra. It indicates that the subband alignment and spacing are identical for both polarities. The negative polarity gain seems to be slightly shifted to higher frequencies. This could be the result of a varying material composition during effect or migration of dopants causing asymmetry electrostatic effects.

5. Conclusion

In this work we demonstrated the potential of symmetric quantum cascade lasers to study the influence of elastic scattering on the device performance. Due to their unipolarity, QCLs can be designed in a way to operate under both polarities. The only difference is the transport direction with respect to the growth direction. The used material system InGaAs/GaAsSb exhibits a pronounced interface asymmetry and is therefore ideal to investigate the role of

interface roughness scattering in QCLs. Inverted interfaces exhibit an increased roughness and cause a stronger influence of interface roughness scattering when electrons are incident on them. We compared the performance of 3 symmetric active regions with different design parameters. One sample shows the most outstanding situation of only unidirectional lasing. The other two samples can be operated with both bias polarities but with significant performance degradation with positive bias. We observe up to 43% lower threshold current densities, 286% higher optical output power and 34% higher maximum operating temperature for negative polarity. Due to their sensitivity on interface roughness scattering, symmetric THz QCLs could also serve as a sensitive test structure to evaluate and improve interface qualities and interface engineering recipes. In addition, they could also be used as a benchmark for testing transport codes since scattering mechanisms can be switched "on and off" by simply changing the bias polarity.

The authors acknowledge partial financial support by the Austrian Science Fund FW (SFB IR-ON F25 and DK CoQuS W1210), the Austrian Nanoinitiative project (PLATON), and the Austrian Society for Microelectronics.